Article

African Vulture Optimization-Based Optimal Control Strategy for Voltage Control of Islanded DC Microgrids

Basma Salah [1,2], Hany M. Hasanien [1], Fadia M. A. Ghali [2], Yasser M. Alsayed [2], Shady H. E. Abdel Aleem [3] and Adel El-Shahat [4,*]

1 Electrical Power and Machines Department, Faculty of Engineering, Ain Shams University, Cairo 11517, Egypt
2 Power Electronics and Energy Conversion Department, Electronics Research Institute, Cairo 12622, Egypt
3 Department of Electrical Engineering, Valley High Institute of Engineering and Technology, Science Valley Academy, Qalyubia 44971, Egypt
4 Energy Technology Program, School of Engineering Technology, Purdue University, West Lafayette, IN 47907, USA
* Correspondence: asayedah@purdue.edu

Abstract: DC microgrids have gained a lot of interest recently due to increasing dc loads such as electric vehicles and the penetration of renewable energy sources (RESs). However, DC microgrids face challenges concerning bus voltage fluctuations, which severely impact the system stability when subjected to uncertainties of load and RESs. This paper focuses on maintaining the stability of a DC-bus through voltage control for a dc islanded microgrid using the concept of cascade double-loop control. The rule in cascade double-loop control is based on a proportional-integral (PI) controller tuned through a new nature-inspired African vulture optimization algorithm (AVOA). The paper presents a comparison of the performance of the African vulture optimization algorithm against particle swarm optimization (PSO) under several operating conditions. The simulation considers actual data for the solar irradiance and temperature and sudden load changes. The system is implemented on MATLAB/Simulink. The results demonstrate that the AVOA-based PI controller performs better in voltage regulation than the PSO-based PI controller.

Keywords: African vulture optimization algorithm; dc microgrid; voltage regulation; renewable energy sources

1. Introduction

Electricity generation is one of the main factors for enhancing a country's economy. At the same time, the traditional usage of fossil fuels has recently led to a greenhouse effect that has polluted the atmosphere [1,2]. As society's awareness increases, governments conduct research to find more pollution-free energy resources to supply the increasing demand. Hence, clean, cost-effective, and environmentally friendly renewable energy sources (RESs) are evolving to resolve traditional resource problems [2,3]. Many renewable energy sources exist in nature, including photovoltaic (PV) cells, wind turbines, tides, fuel cells (FC), and biomass [4]. Rural areas, parking meters, trash compactors, electric vehicle charging stations, electric aircraft, electric ships, and data centers require electrical power, which is why the microgrid (MG) was adopted [5,6]. Microgrids are evolving as a solution for integrating several renewable energy resources and energy storage (ES) systems as batteries [7] to supply such kinds of loads. Microgrids have the advantage of reducing CO_2 emissions, acting as a practical solution for handling the excess energy demand, and limiting the growth of transmission systems which cause severe losses to the system [8].

Microgrids are small power distribution systems connecting multiple distributed generator (DG) units, ES systems, and loads [6]. According to literature, microgrids are classified into direct current (DC) MG, alternating current (AC) MG, and hybrid AC/DC MG [3]. Microgrids have two operation modes: grid and island (off-grid) [7].

The DC microgrid is recently gaining much attention for being efficient with DC sources and dc loads (e.g., electronic loads and electric vehicles). Moreover, DC microgrids have advantages over AC microgrids by removing DC/AC conversion stages and their losses [9]. It also does not have the demerits of frequency and phase synchronization, reactive power flows, and harmonic currents [3,9]. A standalone DC microgrid is off-grid operated depending only on its power sources [1]. Moreover, islanding provides the benefit of improving the microgrid's actual subscribers' actual power quality and reliability [10]. However, it needs a separate control, especially with the RES intermittency and load uncertainties.

ES systems play an essential part in islanded dc microgrids for maintaining their stability during fluctuation and intermittency time of RESs [11,12]. ES systems are devices that store energy generated at a particular moment for use later [12]. The most popular ES units are the batteries or the accumulators [12]. It is also a backup energy source in island (off-grid) mode. When microgrid energy exceeds the load, the excess energy charges the ES unit. The cost of the electrical energy then is lower during the charging period [12]. When microgrid energy is insufficient for the load, the ES system feeds the load with the rest of the energy [3–5,12]. At this time, electrical energy is more expensive during the discharging phase; hence, an ESS helps the power system to run more profitably [12]. The bidirectional converter reduces the ES battery count in the system and maintains the energy supplement to the load [4]. However, there are problems facing the control of this DC-DC bidirectional converter [6]. Moreover, as a DC MG mainly relies on the presence of RESs constrained by weather changes, the traditional controllers face difficulties with the RESs' fluctuations and uncertainties [13]. Furthermore, the DC MG faces voltage profile instability with sudden load disturbances [14].

As science is developing, much research is being done on control strategies for the DC microgrid, to control its dc-link stability and its ES system. Authors in [3] mentioned that research work is under development in controlling ES. A considerable number of control methodologies have been used in literature for maintaining DC/DC converter stability, such as virtual resistors [15] or virtual impedance [16] or adding a capacitor or resistor [17]. However, those techniques have faced problems maintaining stability close to the operating point; they are neither effective nor stable and have high costs [6]. A droop control is a control in which a virtual resistance is connected at the output of each converter [18]. However, this technique has the demerits of inaccurate voltage control and power sharing [18] and the inability to tackle nonlinear issues like load perturbations, which affect the system in transient response [8]. In [19], the author introduced a decentralized control with the intension of accomplishing a control for optimizing energy costs. However, it neglects the DC MG quality of supply plus the demerits of not getting other DGs' shared data [20]. In [21,22], the authors aimed to use traditional droop control for the DC-DC bidirectional converter to achieve power balance between ES systems.

Still, state of charge (SOC) balance control was not accomplished. In [23], a distributed droop control technique is introduced that utilizes centralized communication to get distributed generators (DGs) data to obtain average bus voltage and output current levels to enhance the efficiency of voltage regulation and current sharing. This method suffers from centralized solutions' problems like the single point of failure and the reduced flexibility [23]. Fuzzy logic (FL) controllers are introduced in [24]; however, the FL control systems must be used with the appropriate membership adjustments to perform well. Additionally, the FL control requires expensive processing resources, which causes difficulties during implementation [25]. Advanced control technologies are essential to improve the system by controlling DC/DC converters. Those advanced techniques include predictive model control, sliding mode control, intelligent control, etc., with the merits of being stable, flexible, and robust [6]. Model predictive control is used as an advanced control strategy [26]. However, it suffers from dealing with system constraints [6]. Sliding mode controllers in [6] have good performance with some demerits such as complex design, long computational time, and not being easy to use or maintain. Once the chattering

problem arises, the control can malfunction [27,28]. A PI controller is widely used for being straightforward, maintainable, performing its functionalities, being easy to use and apply [29], and covering large stability margins of operation [30]. Much research has been done to introduce algorithms for better tuning PI parameters. Power taken from the energy sources to feed the dc loads can be optimized by enhancing the voltage profile, which requires implementing an efficient and reliable optimization algorithm to the traditional PI controller, called intelligent control [6], which tunes the controller parameters so that the optimal performance of the system can be reached, maintained over a wide operating range, and there is also no need to represent the model exactly [6].

Moreover, many nature-inspired metaheuristic optimization techniques enhance the voltage profile by controlling the PI controller's parameters. The optimization techniques and algorithms that have been used include particle swarm optimization [31], the water cycle algorithm [32,33], the cuttlefish optimization technique [30], the hybrid cuckoo search with the grey wolf optimization algorithm [34], Harris hawks optimization [35,36], the salp swarm algorithm [37], and the coot bird optimizer [38].

While the intermittent nature of RESs and load uncertainties in power networks raise performance issues and stochasticity [12], the above-mentioned optimization algorithms might not be ideal for maintaining system stability [26,27]. Accordingly, there was a necessity for an advanced robust technique to accommodate those problems and ensure stable operation [26]. The authors were intuited to use the African vulture's optimization algorithm (AVOA). Moreover, this metaheuristic optimization algorithm plays a significant role in satisfying the system requirements. In addition, the AVOA has the advantages of reliability and rapid convergence, which appears through the computational complexity formula $O(N \times (T + TD))$, where T denotes the iteration number and D denotes the problem's dimension, which is better when compared with Harris hawks optimization, which has the complexity $O(N \times (T + TD + 1))$. Furthermore, it has flexibility, simplicity of implementation, robustness, and the ability to maintain the objective function. It can be applied to other grids while keeping the system within the stability constraints.

Based on the above problems, the ES system control strategy and microgrid operation control are studied in this paper. The designed control technique for the ES system presents mitigating voltage profile fluctuations within acceptable limits, and it has a simple design and is considered cost-effective as it mainly depends on the PI controller. Typically, in the off-grid (standalone) mode, to maintain a constant DC-link voltage for the DC microgrid, the primary bidirectional DC/DC converter is controlled. Here, a recommended technique is presented to regulate the ES system's converter to smooth out the PV output and maintain the DC-bus voltage. Finally, optimization-based control for the bus voltage profile is presented by considering practical aspects such as fluctuations of PV power generation and load uncertainty.

Contributions in this paper are accomplished as follows:

(1) This paper introduces PI parameters' tuning for the cascaded linear PI-based control feedback loops using the proposed scheme of the African vulture optimization algorithm (AVOA). It compares its results with the particle swarm optimization (PSO) method to control dc/dc converters.

(2) Adopting the presented PI tuning approach, the DC-bus voltage is maintained with lower settling time and overshoots when subjected to a variable power supply or a sudden consumption pattern. These results reach an overall improvement of above 38%.

This work includes an off-grid (standalone) microgrid's integration of a photovoltaic system, fuel cell system, battery storage system, and DC load simulated using MATLAB/Simulink with the built-in Specialized Technology library.

The rest of the work is presented as follows. Section 2 includes the DC microgrid design and model, while in Section 3, the formulation of the control problem to be applied is presented. Section 4 offers the new nature-inspired metaheuristic AVOA. Section 5

discusses the simulation results of the built-in MATLAB/Simulink, and finally, conclusions are gathered in Section 6.

2. Designing and Modeling of the Microgrid Standalone System

The modeled and simulated DC microgrid system is the PV-battery system presented in [4]. Figure 1 shows the DC microgrid block diagram. The PV with the capacity of 1 kW is connected to a boost converter. In [39], the design for the boost converter is presented that receives its commutation signal from the incremental conductance maximum power point tracking (MPP) to follow the maximum power of the PV [3]. In addition, the FC, with a capacity of 650 W, is connected to the system through a boost converter. That boost converter receives its commutation signal from the AVOA-based PI controller. Then, the battery system with a rated capacity of 150 Ah is connected in parallel to the mentioned DC sources as a backup unit for stabilizing the DC-bus fluctuations through a bidirectional DC/DC converter [4]. In [40], the design for the implemented bidirectional buck-boost converter is presented. The DC microgrid system with a maximum overall capacity of 2.2 kW feeds a dc load represented as a current source drawing power from the system. This paper focuses on controlling the DC/DC bidirectional and DC boost converter to stabilize the DC-bus voltage profile. Controlling those converters is proposed using the AVOA-based PI controller in contrast with the PSO-based PI controller. The AVOA flow chart is presented in Section 4. The computational complexity of the AVOA is $O(N \times (T + TD))$, where T denotes the iteration number and D denotes the problem's dimensions. The robustness of the proposed AVOA is proven through the test scenarios in Section 5. The system is designed to have a bus voltage of 48 V [41] with a voltage deviation of $+/-10\%$ to keep the system stability in the operational state. In addition, the power flow balance is maintained to have the total amount of power generated equal the total power consumed by the load in addition to the power losses and ES units' power [42–47].

$$\sum P_G = P_{Load} + P_{ES} + P_{losses} \tag{1}$$

where P_G is the generated power, P_{Load} denotes the load power, P_{ES} denotes the battery energy storage power, and $P_{loaases}$ denotes the losses power. While satisfying the power flow constraints in which the $P_{min} < P_{PV} < P_{max}$, $P_{Esmin} < P_{ES} < P_{Esmax}$, where P_{PV} denotes the total generated power by PV, P_{max} denotes the maximum generated power by PV = 1.2 Kw, P_{min} denotes the minimum generated power by PV = 0.9 Kw for MPP operation, P_{ES} denotes ES power, P_{ESmin} denotes the minimum ES power = 480 W, and P_{ESmax} denotes the maximum ES power = 550 W. The studied system parameters are shown in Table 1.
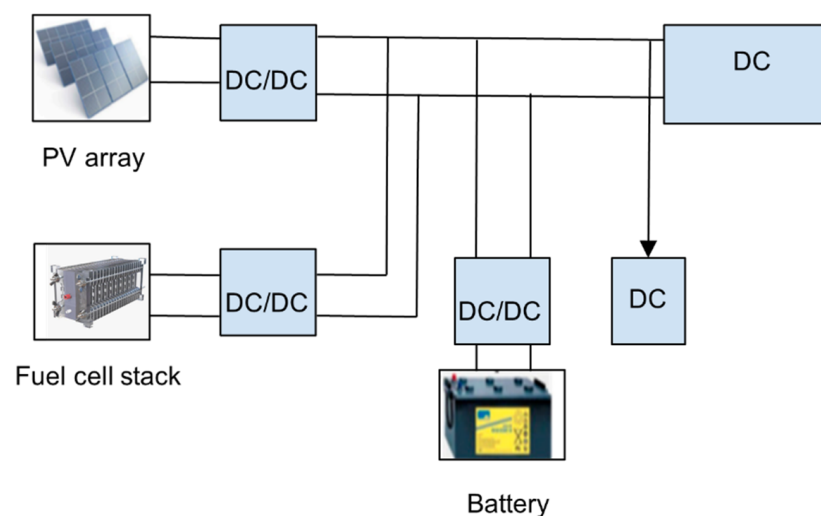

Figure 1. DC microgrid architecture.

Table 1. System dynamic parameters for photovoltaic array, battery, and DC load.

DC Microgrid	
Nominal voltage	48 V
Photovoltaic array parameters	
Series modules/string count	1
Parallel strings count	5
Short circuit current of the module at standard test conditions	7.84 A
Open-circuit voltage of the module at standard test conditions	36.3 V
MPP current of the module at standard test conditions	7.35 A
MPP voltage of the module at standard test conditions	29 V
Module maximum power	213.15 W
Inductor value for the PV boost DC/DC converter	1.5 mH
Capacitor value for the PV boost DC/DC converter	3300 μF
Switching frequency value for the PV boost DC/DC converter	5000 Hz
Battery parameters	
Battery type	Lithium-Ion
Nominal voltage	24 V
Battery capacity rating	150 Ah
Inductor value for the battery bidirectional DC/DC converter	0.5 mH
Series resistor value for the battery bidirectional DC/DC converter	0.1 Ω
Capacitor value for the battery bidirectional DC/DC converter	2 mF
Shunt resistor value for the battery bidirectional DC/DC converter	10 μ Ω
DC load	
Constant resistance	4.8 Ω
Constant power	480 W

2.1. Photovoltaic Modeling

In the designed DC microgrid, PV cells are the main RESs for a number of reasons such as PV panels' falling costs, a vast number of applications, PV modules' sizing flexibility, and PV modules' rising effectiveness [48]. Those PV cells are connected to a DC/DC boost converter to feed the dc load. This DC/DC converter has its control signal from maximum power point tracking. A semiconductor called PV cells utilizes sunlight to generate energy. The entering photons that must be absorbed must have greater energy than the cell's bandgap. The absorbed photon produces pairs of mobile charge carriers (hole and electron), which are kept apart by the device's p-n junction (diode) structure. A potential difference is introduced due to this action, causing the electric current to be generated. The current source's current is directly proportional to the amount of light the PV cell is exposed to [48].

Since the accuracy of the PV directly relies on the design. Solar PV has equivalent circuits such as the single-diode, double-diode, and triple-diode models. However, double-diode and triple-diode are not famous for their complex architecture [48]. Therefore, the PV equivalent circuit is represented in this work by the single-diode circuit shown in Figure 2, which is mainly used for being straightforward, functioning, and easy to implement [3,4,49]. The circuit is composed of a photo-generated current source parallel to a single diode, a series resistor (R_s), and a parallel resistor (R_p).

The PV conversion efficiency is directly affected by a slight change in R_s. If R_s decreases, the PV output decreases. All series resistances, including the resistance of the metal grid, contacts, and current-collecting wires, are all represented by the R_s [48], while current leakage within the PV cell circuit is defined by R_p [48]. In [3,27], the equation of the output current of the PV unit is expressed as

$$I_{pv} = I_{gen} - I_{diode} - I_p \tag{2}$$

$$I_{pv} = I_{gen} - I_0 [e^{\frac{V_{pv} + I_{pv}R_s}{A}} - 1] - \frac{V_{pv} + I_{pv}R_s}{R_p} \tag{3}$$

where I_{gen} is the PV generated current, I_{diode} is the current passing in the diode, I_p is the current leakage in the shunt resistor, R_s is the cell's series resistance, R_p is the cell's shunt resistor, A is the ideality factor, and V_{pv} is the cell's output voltage. The PV voltage output of each cell is represented by Equation (4) in [49].

$$V_{pv} \approx \frac{A * K * T_c}{e} ln(\frac{I_{gen} + I_{diode} + I_{pv}}{I_{diode}}) - R_s I_{pv} \qquad (4)$$

where I_{pv} stands for the cell's output current, I_{gen} for the photocurrent, I_{diode} for the diode's reverse saturation current, R_s for the cell's series resistance, T_c for the cell's operating temperature, A for the ideality factor, and V_{pv} for the cell's output voltage. The PV array is formed by the connections of series and parallel combinations of the PV cells; consequently, Equation (2) is affected by this combination according to [3]. The array used in the microgrid here is simulated using the MATLAB Specialized Technology library. The used solar PV cell parameters are set from the PV array built-in in the MATLAB Specialized library. Configuration of the PV model is done by specifying the irradiance and temperature data.
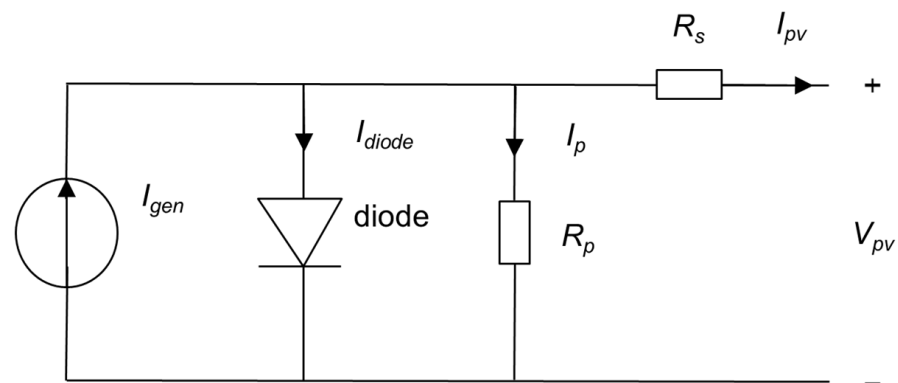

Figure 2. PV equivalent circuit.

2.2. Maximum Power Point Tracking

This control mechanism is applied to the boost converter of the PV array. The PV array output varies with the changes in temperature and irradiance during the day. Thus, there was a need to optimize the PV output power. Throughout the various methodologies introducing the MPPT, incremental conductance (IC) was chosen for its fast response and better determination of the MPPT despite the irradiance and temperature changes [3]. MPP is at zero difference for the power derivative to the voltage derivative [3]. The equations for MPP are

$$P = V * I \qquad (5)$$

$$\partial P / \partial V = I * \partial V / \partial V + V * \partial I / \partial V \qquad (6)$$

$$At\ MPP\ \partial P / \partial V = 0 \qquad (7)$$

$$so,\ \partial I / \partial V = -I / V \qquad (8)$$

where P is the PV output power, V is the output voltage of PV, I is the output current of PV, ∂P is the power derivative, ∂V is the voltage derivative, and ∂I is the current derivative.

2.3. Boost Converter

The boost converter dynamic model, as in Figure 3, is described via equations in [18] that utilize Kirchhoff laws, as in

$$L_i * i_L^{\cdot} = U_i - (1 - u_i) * V_i \qquad (9)$$

$$C_i * V_i^{\cdot} = (1 - u_i) * i_L - I_i \qquad (10)$$

where U_i is the source output voltage, u_i is the control input in the range of [0, 1], V_i is the output boosted voltage, i_L is the inductor current, i_i is the output load current, L_i is the inductance, and C_i is the capacitance, where $i \in \{1, 2, \ldots\}$. According to [39], the inductance and capacitance values of the boost converter are depicted from the following:

$$L = \frac{U * (V - U)}{f_s * \Delta I * V} \tag{11}$$

$$C = \frac{(I * D)}{f_s * \Delta V} \tag{12}$$

where f_s is the switching frequency, ΔI is the current ripple, I is the output load current, ΔV is the output voltage change (ripples), U is the source output voltage, V is output boosted voltage, and D is the duty ratio. Thus, the load voltage can be derived as follows, depending on the load type. In our case, load type is a constant current load. The steady-state conversion ratio is mentioned in [50] as

$$V = \frac{U}{1 - D} \tag{13}$$

where U is the source output voltage, V is output boosted voltage, and D is the duty ratio. The magnitude of input current ripple is

$$\frac{U * D}{f_s * L} \tag{14}$$

where f_s is the switching frequency, U is the source output voltage, D is the duty ratio, and the output voltage ripple is

$$\frac{I * D}{f_s * C} \tag{15}$$

where f_s is the switching frequency, I is the output load current, C is the capacitance of the boost converter, and D is the duty ratio. The PV array output voltage is 25 V, which is then boosted to 48 V.
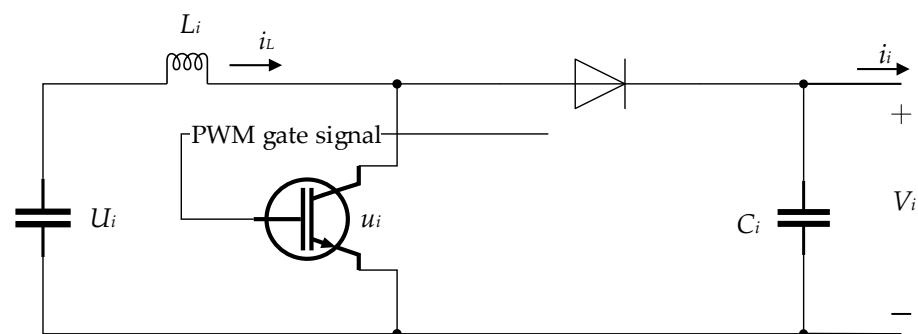

Figure 3. Boost converter.

2.4. Fuel Cell Modeling

Fuel cells are considered green energy for not having carbon dioxide emissions [29]. Fuel cells have the following advantages: high power densities and high power conversion efficiencies [51]. However, the fuel cell has a complex architecture, so the authors in [52] suggested controlling voltage and current through PID tuned with optimization algorithms. Since system efficiency frequently depends on power DC/DC converter performance while power consumption changes, applying a robustness control strategy is imperative to ensure the operation of the FC's DC/DC power converters [29]. In [29], the authors mentioned that the lower modeling accuracy was obtained when fuzzy control was used, and system control failed with load uncertainties when linear quadratic regulator (L.Q.R.) control was applied.

FC is considered an energy conversion system that can transform chemical energy into electrical energy using an electro-mechanical combination of oxygen and hydrogen [49]. That conversion process produces the purest byproduct, water, as a side product [53]. These cells are trustworthy, dependable, efficient, and safe. The electrolyte acts as a separating medium between the negative electrode, or anode, and the positive electrode, or cathode, in the FC's basic operating principle. Electrochemical oxidation occurs when fuel is put into the anode (if the fuel is hydrogen), and electrochemical reduction occurs when an oxidant is introduced into the cathode chamber [53]. The hydrogen that is pumped into the anode chamber breaks down with the aid of a catalyst to produce hydrogen ions and electrons. As oxygen is injected into the cathode chamber, hydrogen ions, electrons, and oxygen combine to form water.

The number of free electrons produced when oxygen and hydrogen chemically interact at the cathode and anode with the existence of ceramic electrodes determines the fuel cell's output current. Due to a current limitation caused by a lack of hydrogen that reacts to produce energy, the FC's power output is constrained. Figure 4 represents the equivalent circuit of the fuel cell, as presented in [49].
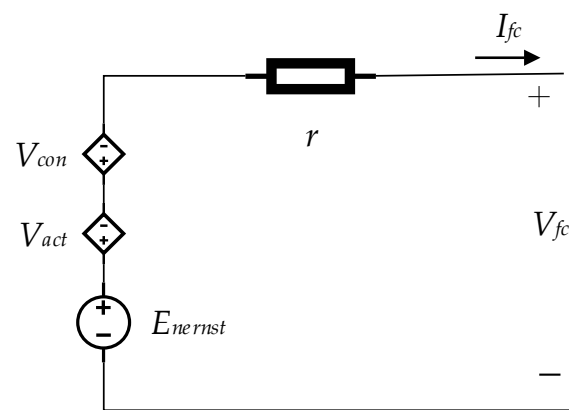

Figure 4. Fuel cell equivalent circuit.

The potential difference of FC's stack between the electrodes is calculated through Ohm's law and the Nernst equation in (16), in which series FCs are connected [53]. There are three voltage values in each fuel cell: the concentration voltage (v_{con}), the ohmic voltage drop (v_{ohmic}), and the activation voltage (v_{act}) [53].

$$V_{fc} = N_o[E_{nernst} - v_{con} - v_{act} - v_{ohmic}] \tag{16}$$

$$E_{nernst} = 1.229 - 0.85 * 10^{-3}(T_{fc} - 298.15) + 4.3085 * 10^{-5} * T_{fc} * lnP_{H_2}P_{O_2}^{\frac{1}{2}} \tag{17}$$

$$v_{ohmic} = r * I_{fc} \tag{18}$$

$$v_{con} = -\beta \, ln(1 - \frac{J}{J_{max}}) \tag{19}$$

$$v_{act} = -\left[\xi_1 + \xi_2 T_{fc} + \xi_3 T_{fc} ln(C_{o_2}) + \xi_4 T_{fc} ln(I_{fc})\right] \tag{20}$$

where V_{fc} is the output voltage of the fuel cell stack, N_o is the number of cells in series in the stack of the fuel cell, r is the fuel cell resistance, E_{nernst} is the FC reversible voltage, T_{fc} is the temperature of the FC, ξ_{1-4} are the semi-empirical values, β is a constant value, J, J_{max} are the current density real and maximum parameters, P_{H_2}, $P_{O_2}^{\frac{1}{2}}$ are the partial pressure of the hydrogen and oxygen, respectively, and I_{fc} is the output current of the FC. The FC used has the parameters given in Table 2.

Table 2. Fuel cell characteristics.

Fuel Cell Parameters	
Nominal current	30 A
Nominal voltage	22.23 V
Boost converter inductance	0.5 mH
Boost converter capacitance	4000 µF

The fuel cell output voltage is then boosted to the DC-link voltage of 48 V.

2.5. Battery Energy Storage System

As an impact on the nature of RESs intermittency in the off-grid DC microgrid, it might be above or below the required energy by the load. Thus, the battery energy storage (BES) source becomes vital for stabilizing the load voltage profile. The batteries have various types, as in [11]. Lithium-ion batteries with an equivalent circuit in Figure 5 are chosen for having adequate energy capacity, maintainability, a reasonable life span [3] of 5–15 years, least-cost operation, and high efficiency of up to 97% with safe operation [54]. Battery sizing relies upon several factors, including the time needed to supply the load without recharging [55]. The battery's permitted depth of discharge (DOD) is another crucial aspect that is considered while sizing the battery.
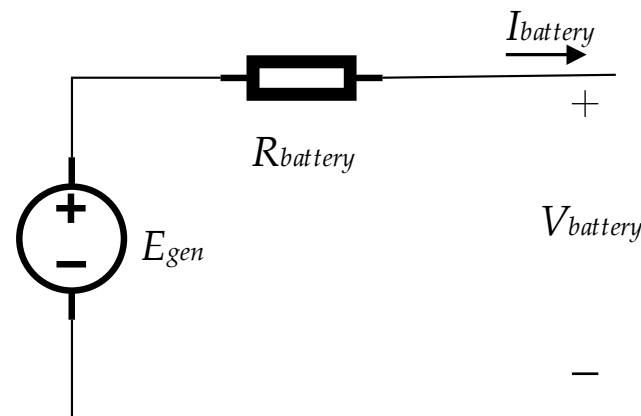
Figure 5. Equivalent circuit for battery.

Moreover, it is crucial to maintain batteries at 25 °C to strengthen their lifespan. Additionally, at this temperature, the derate factor (D_f) will be equal to 1. Equation (22) describes the battery capacity calculation. While the following equation describes the battery output voltage.

$$V_{battery} = E_{gen} - I_{battery} * R_{battery} \tag{21}$$

where $V_{battery}$ is the battery output voltage, E_{gen} is the generated no-load voltage, $R_{battery}$ is the internal resistance, and $I_{battery}$ denotes the battery current. The modeled battery is simulated using the built-in model in the MATLAB Specialized Technology library.

$$C = \frac{L * D_n}{DOD_{max} * D_f} \tag{22}$$

where D_n is the number of autonomous days, DOD_{max} is the maximum depth of battery discharge, D_f is the derate factor, C is the required battery bank capacity (Ah), and L is the supplied load throughout the day (Ah/day).

2.6. Bidirectional Buck-Boost DC/DC Converter

Designing the converter is as mentioned in [40] in Figure 6. To maintain the stable charging and discharging process, the bidirectional DC/DC converter is controlled. The controller block diagram is as follows in Figure 7. The inductance value is designed as mentioned according to [40] as in the following equation

$$L = D * (1 - D)^2 * V_h^2 / (2 * P_c * f) \tag{23}$$

where D is the duty cycle, V_h is the high voltage side = 48 V, P_c is the critical light load = 480 W, and f is the switching frequency = 15,000. To maintain the operation in the continuous conduction mode, the previous inductance value is multiplied by 1.25. Capacitance values are calculated from the following equations

$$C_h = D / (R_h * f(\Delta v_h / v_h)) \tag{24}$$

$$C_l = (1 - D) / (8 * \frac{\Delta v_l}{v_l} * L * f^2) \tag{25}$$

where C_h is the high voltage side capacitance, C_l is the low voltage side capacitance, Δv_h is the high voltage side ripples, L is the inductance value, Δv_l is the low voltage side ripples, and v_l denotes the low voltage.
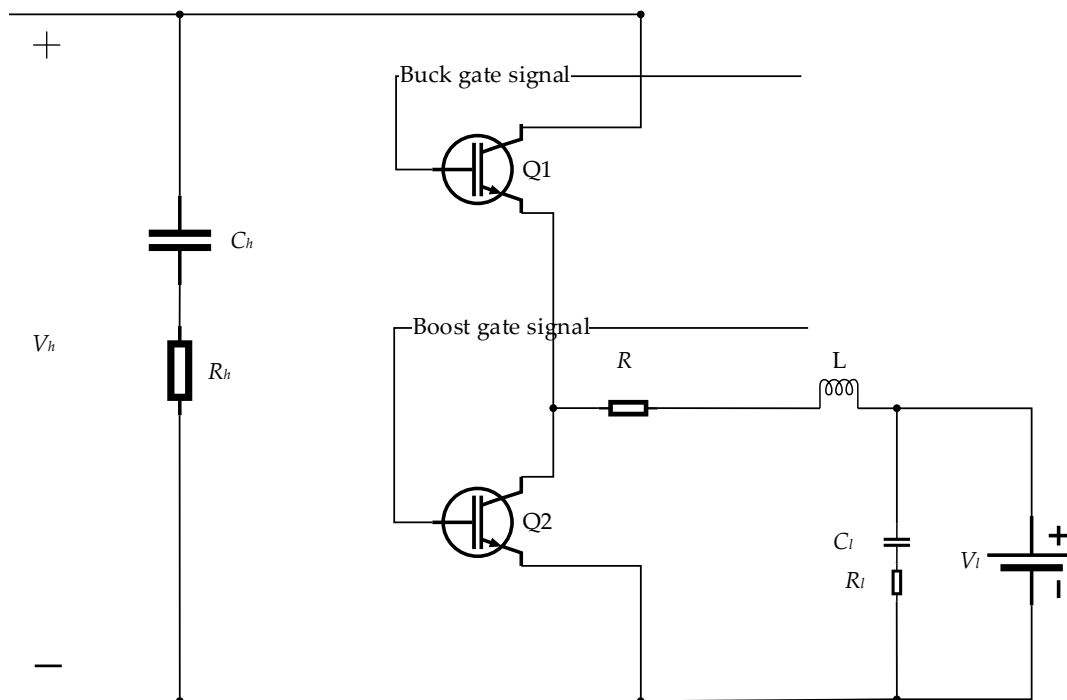

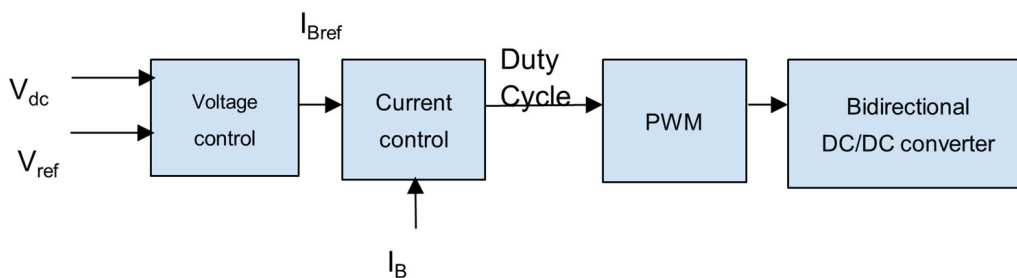**Figure 6.** Bidirectional buck-boost converter.

Figure 7. Closed cascade double-loop control block diagram.

Proportional-Integral Controller

Minimizing the steady-state error is handled by this controller to maintain the system operating in the stability zone by keeping the DC-link voltage within the acceptable limits. The following equation describes the PI controller as mentioned in [56].

$$G\left(s\right) = k_p * \left[1 + \left(1/sT_i\right)\right] \tag{26}$$

where K_p is the proportional gain factor, and T_i is the integral time constant of the controller.

The PI controller input is the error resulting from comparing the reference 48 V with the dc-link voltage. Then, the output of this controller is fed to another PI controller to be compared with the battery current. Then, the output signal is compared with a sawtooth wave with a frequency of 15,000 Hz to get the PWM signal for operating the IGBTs of the bidirectional buck-boost converter, as described in Figure 6.

3. Voltage Control Based on PI Controllers

As mentioned previously, the system uses cascaded double-loop control formed from two PI controllers for controlling the bidirectional DC/DC converter of the BES system and one PI controller for controlling the boost DC/DC converter of the FC. Tuning these controllers is applied through the advanced control technique of the AVOA. The controller mathematical formulation is described in [27]:

$$G(s) = K_p + \frac{K_i}{s} \tag{27}$$

where K_p is the proportional gain factor that minimizes the rise time parameter and K_i is the integral gain factor that minimizes the steady-state error parameter. The voltage regulation problem is described by relying on the integral square error (ISE) methodology as an objective function. The ISE cost function is minimized in all optimization methods. The minimization of the ISE for the microgrid system is the objective function of applying this technique, and integrating the system error square over a predetermined amount of time results in an estimate of system performance. With keeping the constraints of the K_p and K_i within the predefined boundaries, $0 < k_p < 10$, $50 < k_i < 150$ for the two PI controllers of the bidirectional converter for the ES, and $0 < k_p < 0.01$ and $0 < k_i < 0.4$ for the PI controller of the boost converter for the FC, while maintaining the voltage deviation within $+/-10\%$ to keep the system stability in the operational state.

$$\text{ISE} = \int_0^{t_s} \{\Delta V^2 + \Delta I^2\}dt \tag{28}$$

where ΔV^2 is the voltage difference = $V_{load} - V_{ref}$, ΔI^2 is the current difference = $I_b - I_{bref}$, and t_s is the time to run the simulation.

4. African Vulture Optimization Algorithm

For the limited capability of mathematical methods to get optimal parameters, meta-heuristic optimization algorithms are used. Metaheuristic algorithms are based on observing and analyzing nature's creatures' attitudes. They are easy to implement, easy to learn, flexible for several problems without needing to change the algorithm code, and can reach optimal global solutions [57].

The proposed algorithm in this work is the African vulture optimization algorithm (AVOA), inspired by their search for food. Vultures are predatory birds that aim to hunt injured or ill animals. This bird helps to keep the carcasses from being infected. The algorithm flowchart is shown in Figure 8. The algorithm considers the following assumptions: for the N number of vulture population searching for food, vultures are split into two groups, where each vulture calculates fitness so that we have the best solution and the second-best solution in which one of them is replaced, as the groups have various capabilities for searching for food. The anti-hunger vultures are considered the weakest

and the most starving at the formulation stage. Others are escaping far from them to get to the optimal solutions [57].

4.1. Initialization Stage

The population is spread over the search area:

$$Position = rand(N,1) * (ub - lb) + lb \tag{29}$$

where *rand* is a random value in a range of [0, 1], u_b is the upper limit, l_b is the lower limit, *N* is the number of vulture population, and *Position* is the solution parameters for each search agent.

4.2. Calculate Fitness

The fitness of each vulture in the population for each iteration is calculated to get the optimal best solution in the first group, and the optimal second best is the best solution for the second group for each iteration. For each group, the best solution is obtained from the probability Equation (30) through the Roulette wheel, and this probability is within [0, 1].

$$p_i = \frac{F_i}{\sum_{i=1}^{n} F_i} \tag{30}$$

4.3. Vultures Behavior

As mentioned, the starved vultures are the weakest, so they search for food close to the strongest ones and are aggressive as their energy is not enough to make a far proper search with the *z* value less than 0. This is shown in Equation (31).

$$F = (2 * rand_1 + 1) * z * (1 - it/maxIT) + h * (sin(\frac{\pi}{2} * \frac{it}{maxIT}) + cos(\frac{\pi}{2} * \frac{it}{maxIT}) - 1) \tag{31}$$

where *F* is the not hungry vulture, *it* is the iteration number, *maxIT* is the total iterations, *z* represents a random number within range [−1, 1], *h* is a random number within range [−2, 2], and $rand_1$ is a random number in a range of [0, 1]. The second part of the above equation avoids optimal local convergence and improves this algorithm's reliability. If *F* has a value above 1, the vulture gets into the exploration phase to try to find the solution in another region, while if the value is below 1, the vulture enters the exploitation phase, which focuses on the accuracy enhancement of the resulting solution.

4.4. Exploration Phase

Vultures search for random food regions based on two approaches, and having the parameter p_1 in [0, 1] helps to select which approach to follow. The exploration phase has a value $rand_{p1}$ in [0, 1] that is compared to p_1 according to Equations (32) and (33) to select the proper approach to searching. Equation (32) means the vulture's search is close to one of the best solutions obtained, which occurs when $rand_{p1} >= p_1$. Equation (33) means vultures search in a new far area in the environment, which happens when $rand_{p1} < p_1$.

$$L(i+1) = R(i) - F + rand_2 * (u_b - l_b) * rand_3 + l_b \tag{32}$$

$$L(i+1) = R(i) - (|X * R(i) - L(i)| * F) \tag{33}$$

where $L(i+1)$ is the preceding iteration vulture location, *F* is the calculated satiation rate in Equation (31), *R(i)* is among the top solutions selected based on Section 4.2, *X* is the random number that detects the random motion of the vulture for the food protection process equaling 2 x *rand*, (*rand*, $rand_2$, $rand_3$) are random numbers within [0, 1], ub is the upper limit, l_b is the lower limit, and *L(i)* is the current iteration vulture location.

4.5. Exploitation Phase

The exploitation phase is divided into two stages, each with two approaches. One of the approaches in each stage is selected through the attributes p_2 and p_3, having values in [0, 1]. If F is above 0.5 and less than 1, the vulture is in the first stage of exploitation (competing over food). The first stage has two approaches: rotating flight and siege-fight. Based on p_2, one of them is selected. Having p_2 greater than or equal to $rand_{p2}$, a rotating flight is chosen and follows Equation (34), or having p_2 smaller than $rand_{p2}$, siege-flight is selected following Equation (37). The rotational flight is expressed by
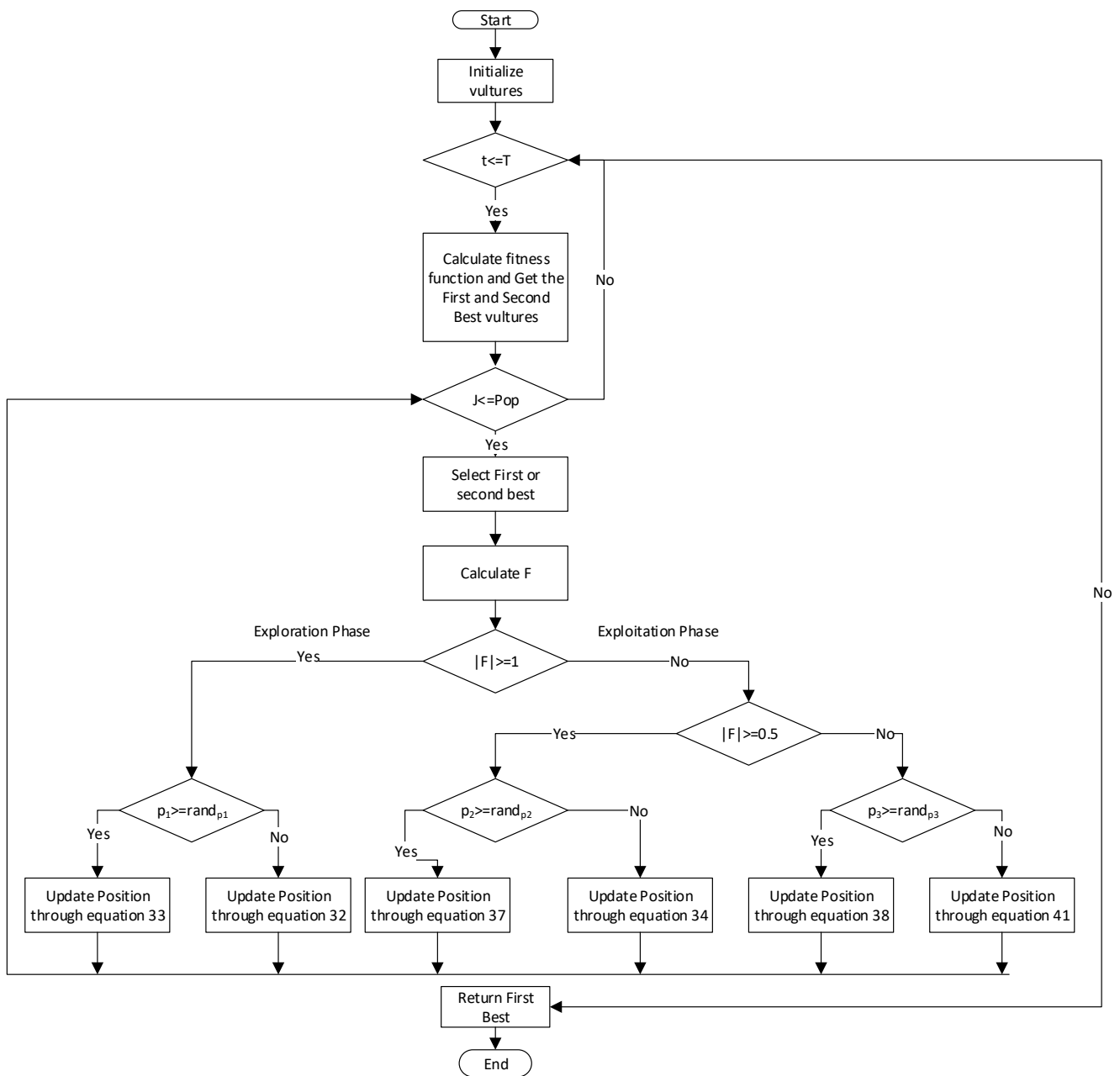
$$L(i+1) = R(i) - (S_1 + S_2) \tag{34}$$

Figure 8. Flowchart of AVOA.

where

$$S_1 = R(i) * \frac{rand_5 * L(i)}{2\Pi} * cos(L(i)) \tag{35}$$

$$S_2 = R(i) * \frac{rand_6 * L(i)}{2\Pi} * sin(L(i)) \tag{36}$$

$L(i + 1)$ is the updated location for the vulture, $R(i)$ denotes one top solution selected in Section 4.2, ($rand_5$ and $rand_6$) are random numbers within [0, 1] range, while (sin, cos) are mathematical functions.

$$L(i + 1) = |X * R(i) - L(i)| * (F + rand_4) - d \tag{37}$$

where $d = R(i) - L(i)$ is the vulture's distance from one of the two groups' best vultures, $L(i)$ is the present location, $R(i)$ denotes one top solution selected in Section 4.2, $rand_4$ is random numbers within [0, 1] range.

The second exploitation stage involving competition for food is either a fierce siege-fight or assembling a variety of vultures around the feeding source, based on the p_3 value. When $rand_{p3} >= p_3$, assembling vultures over food takes place and follows Equation (38), and when $p_3 > rand_{p3}$, fierce competition happens in the following Equation (41).

$$L(i + 1) = \frac{A_1 + A_2}{2} \tag{38}$$

$$A_1 = best_1 - \frac{best_1 * L(i)}{best_1 - L(i)^2} * F \tag{39}$$

$$A_2 = best_2 - \frac{best_2 * L(i)}{best_2 - L(i)^2} * F \tag{40}$$

where A_1 and A_2 represent vulture motion, $best_1$ denotes the present iteration's top in the first group, $best_2$ denotes the current iteration's top in the second group, F is the calculated satiation rate in Equation (31), $L(i)$ is the present location, and $L(i + 1)$ is the updated vulture location.

$$L(i + 1) = R(i) - |d * F * LF| \tag{41}$$

$$\text{where } LF = 0.01 * \frac{u * \sigma}{|v|^{\frac{1}{\beta}}} \tag{42}$$

$$\sigma = \left(\frac{\Gamma(1 + \beta) * sin\left(\frac{\pi\beta}{2}\right)}{\Gamma(1 + \beta) * \beta * 2 * \left(\frac{\beta - 1}{2}\right)} \right)^{\frac{1}{\beta}} \tag{43}$$

where β is fixed at 1.5, u and v are numbered in [0, 1], $d = R(i) - L(i)$ is the vulture's distance from one of the two groups' best vultures, $L(i)$ is the present location, and $R(i)$ denotes one top solution selected in Section 4.2.

5. Simulation Results

As presented earlier, the system is modeled on MATLAB/Simulink integrated with code in m-files. To solve the optimization problem, the PV-battery islanded microgrid simulation system interfaces with the optimization algorithms through m-files in MATLAB. Our main simulation test scenarios focus on the RESs uncertainties (including PV and fuel cell) and sudden load changes. The PV-battery system consists of 1 kW solar power integrated with a battery of 150 Ah capacity connected to a load with 480 W nominal value.

5.1. Case #1: Sudden Load Changes

In [56], a sudden step load change is applied. Through performing this scenario, the load is step changed from 480 W to 720 W (50% load increase at time = 1 s) while

neglecting the effect of the RESs uncertainties in this scenario and maintaining the STC values for irradiance at 1000 W/m^2 and temperature at 25 °C. The output performance proposed algorithm (AVOA) is compared with the PSO algorithm to verify its validity in our system. The statistical measurements performed on 10 independent runs, as mentioned in Table 3, show the robustness of the new algorithm. The higher-order parameters for the optimizers are obtained through trial and error, including multiple runs for the optimizers. Fifty population sizes represent those parameters in 100 iterations for the AVOA and ten particles in 100 iterations for PSO. Figure 9 shows the convergence curves of the AVOA against PSO, in which the AVOA has a lower fitness value than PSO. Moreover, the search area for the swarm particles and vulture population is kept at $0 < k_p < 10$, $50 < k_i < 150$ for fair comparisons. Table 4 shows the PI controllers' gain parameters obtained from the applied optimizers.

Table 3. Statistical performance measurements for AVOA on the PV-battery system.

Factor	ISE.
Average	0.0739
Median	0.0702
Standard deviation	0.0109
Variance	0.0001
Minimum	0.0702
Maximum	0.1067
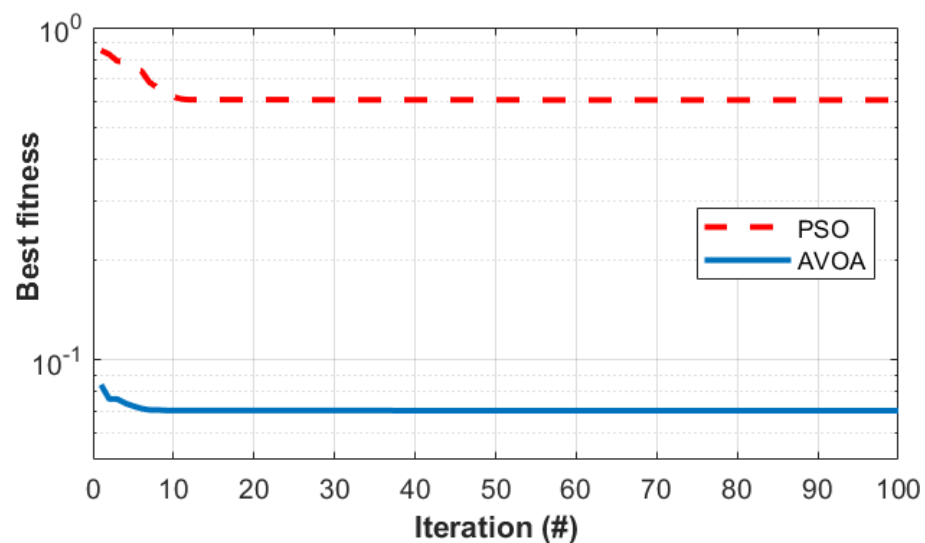
Figure 9. Convergence curves of PSO and AVOA.

Table 4. Microgrid's PI controller parameters.

Gains	AVOA-Based		PSO-Based	
	PI$_1$	PI$_2$	PI$_1$	PI$_2$
K_p	10	0.0271	6.6912	0.5006
K_i	150	80.1196	70.6795	58.1476

The simulation output in Figure 10a,b indicates the lower overshoot and settling time for the AVOA on the load voltage. The transient factors of maximum percentage overshoot (MPOS), maximum percentage undershoot (MPUS), and settling time (T$_s$) are the indicators used to assess the AVOA. These indicators have lower values for the AVOA when compared to those of the PSO. The results are presented in Table 5. These results indicate that the MPOS has decreased by almost 38% in the case of the AVOA than in the

case of the PSO. Moreover, the results present the decrease in the MPUS in the case of the AVOA in contrast with the PSO to be 39%. Furthermore, the reduction in the settling time in the proposed AVOA compared to the PSO is almost 41%.
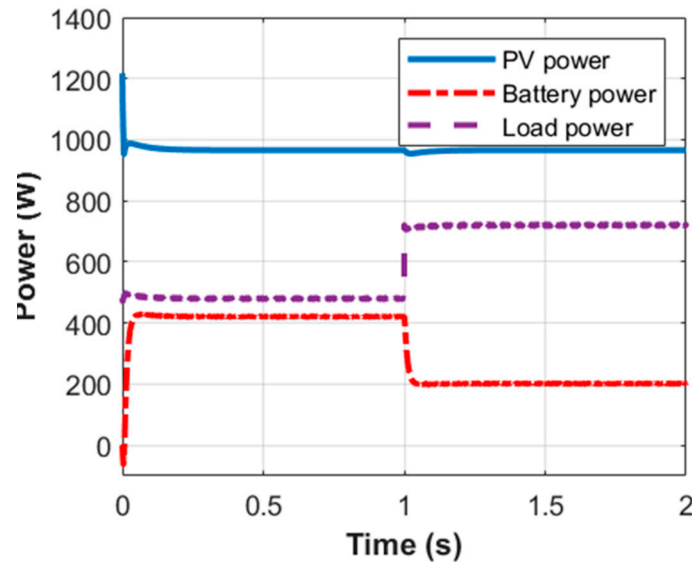
(**a**) PV, Battery, and Load power
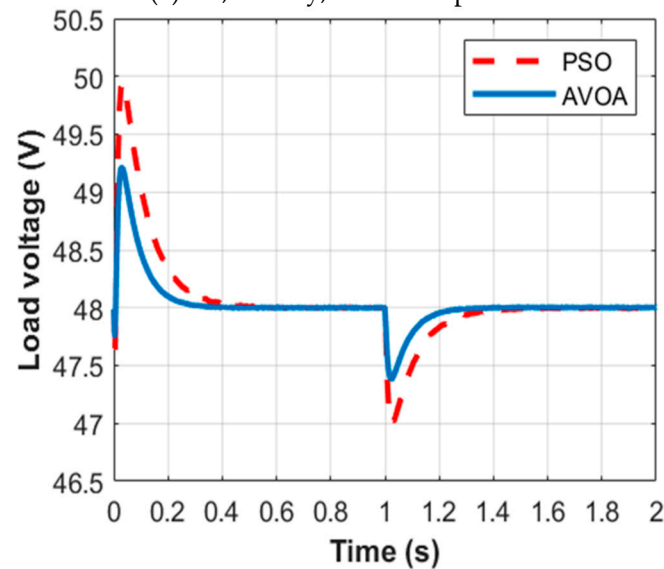
(**b**) Load voltage change

Figure 10. (**a**) PV, battery, and load power; (**b**) load voltage change.

Table 5. Microgrid's transient parameters for load voltage.

	MPOS (%)	MPUS (%)	T_s (s)
AVOA	2.5208	1.2708	0.38
PSO	4.0625	2.0833	0.64

5.2. Case #2 RESs Uncertainties

The authors in [58] tested the system against RESs changes through a step-change in irradiance without considering load change or temperature change. Figure 11a shows the step changes of the irradiance from 1000 W/m^2 to 750 W/m^2 at time = 1 s, then at time = 2 s increased from 750 W/m^2 to 900 W/m^2 and at time = 3 s increased from 900 W/m^2 to 1000 W/m^2. Figure 11b represents the PV, battery, and load powers with the impact of step

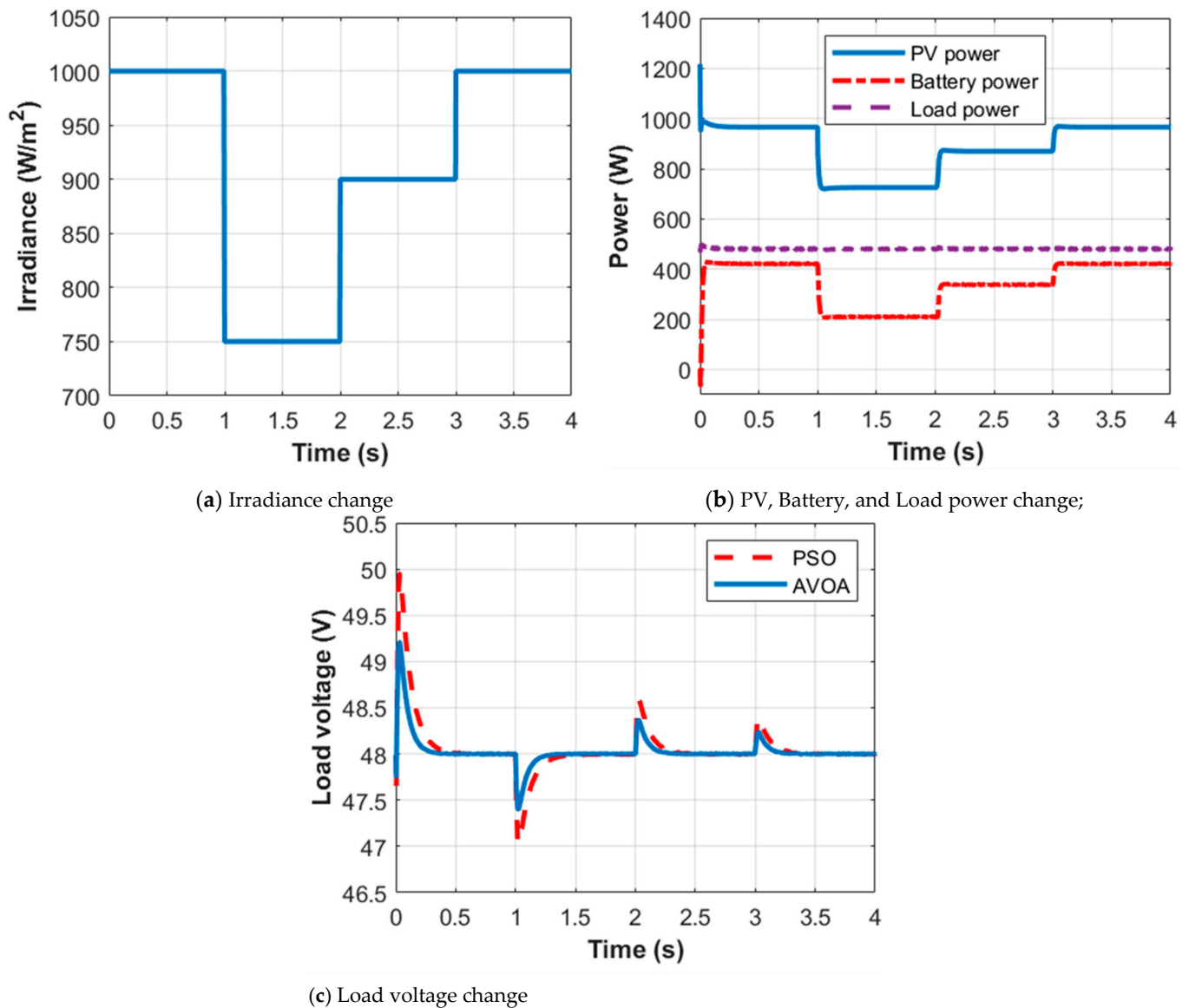irradiance fluctuations. Figure 11c represents the irradiance change impact on load voltage.

(**a**) Irradiance change

(**b**) PV, Battery, and Load power change;

(**c**) Load voltage change

Figure 11. (**a**) Irradiance change; (**b**) PV, battery, and load power change; (**c**) load voltage change.
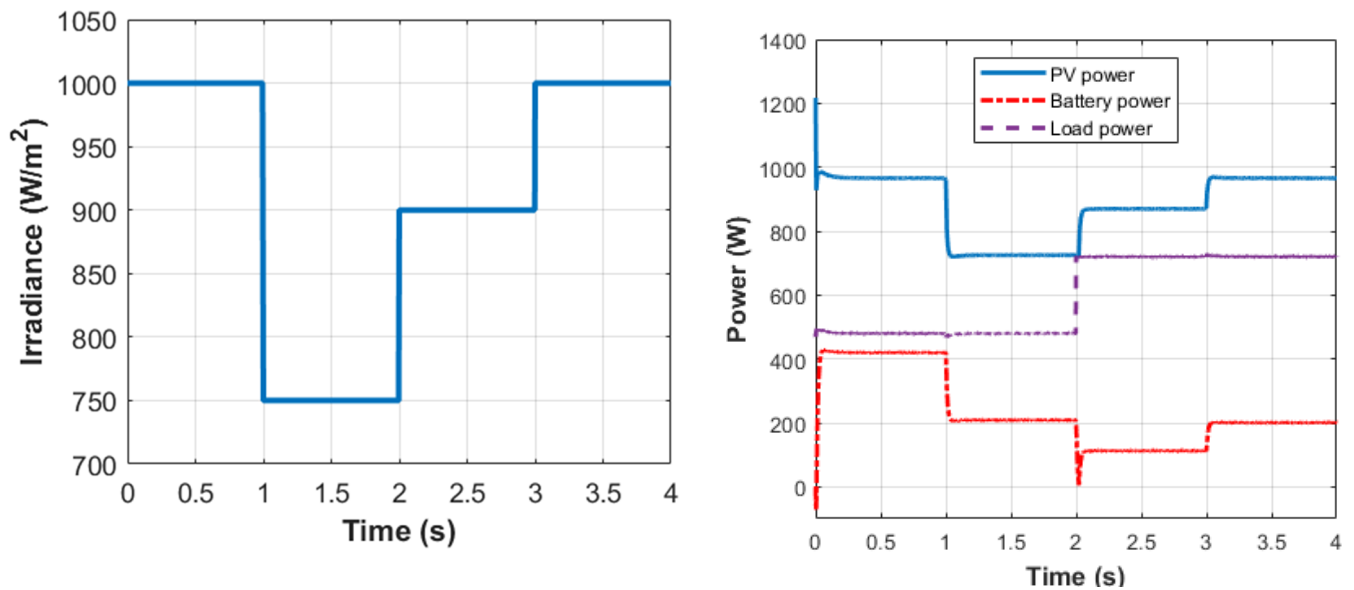
The resulting outcomes showed better performance for the AVOA in contrast with the PSO on the system load voltage parameter through the indicators used to assess its performance. Those indicators are presented in Table 6. The MPUS is 1.25% with the AVOA while the MPUS is 2.02% with PSO, which indicates a MPUS enhancement by almost 38.12%. While the MPOS is 2.52% with the AVOA and 4.0625% with PSO, this presents an improvement in the MPOS by about 38%. Furthermore, T_s is 0.36 s with the AVOA while T_s is 0.59 s with PSO, so T_s has intensified by nearly 39%.

Table 6. Microgrid's transient parameters for load voltage.

|	MPOS (%)	MPUS (%)	T_s (s)
AVOA	2.52	1.25	0.36
PSO	4.0625	2.02	0.59

5.3. Case #3: RESs Uncertainties Accompanied by Load Disturbances

Here, the authors test the system against RESs changes through a step-change in irradiance, considering load change while not considering temperature change. Figure 12a shows the sudden variations of the irradiance from 1000 W/m^2 to 750 W/m^2 at time = 1 s, followed by an increase from 750 W/m^2 to 900 W/m^2 at time = 2 s and then at time = 3 s raised again from 900 W/m^2 to 1000 W/m^2. Load increases suddenly by 50% at time = 2 s. Figure 12b represents the PV, battery, and load powers with the impact of step irradiance fluctuations accompanied by load step changes. Figure 12c represents the irradiance and load change impact on load voltage.

(**a**) Irradiance change

(**b**) PV, Battery, and Load power change
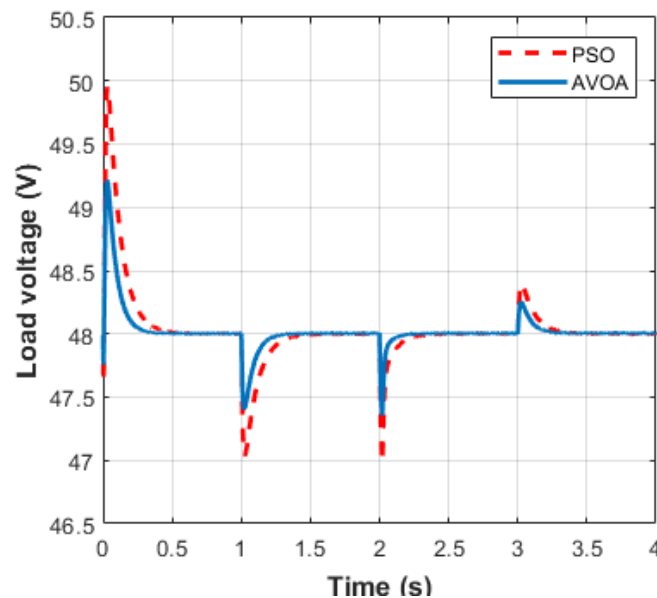
(**c**) Load voltage change

Figure 12. (**a**) Irradiance change; (**b**) PV, battery, and load power change; (**c**) load voltage change.

The main outcome of this case is that it shows a better performance for the AVOA in contrast with the PSO on the system load voltage parameter through the indicators used to assess its performance in Table 7. Those indicators show an enhancement in the MPUS, MPOS, and T_s with 36.6%, 37.84%, and 56.25% values for the AVOA over the PSO. Considering the MPUS, which is 1.341% with the AVOA and 2.115% with PSO, this suggests an almost 36.6% improvement in the MPUS. The MPOS has improved by around 37.84%, with a MPOS of 2.529% with the AVOA and a MPOS of 4.0688% with PSO. T_s has also enhanced by over 56.25% as it was 0.48 s with the AVOA and 0.75 s with PSO.

Table 7. Microgrid's transient parameters for load voltage.

|	MPOS (%)	MPUS (%)	T_s (s)
AVOA	2.529	1.341	0.48
PSO	4.0688	2.115	0.75

5.4. Case #4: RESs Uncertainties with Actual Data

Irradiance and temperature change through actual data obtained from the website of NREL at the Solar Radiation Research Laboratory [59] on June 8, 2022, were applied to our Simulink system while excluding the load uncertainties impact in this case and maintaining load at 480 W. The data were recorded in a day from 4:30 am to 7:30 pm, with minute changes in Figure 13a–b. Irradiance varies smoothly from 8.5496 W/m^2 to 1045.07 W/m^2, while temperature fluctuates continuously from 10.33 °C to 25.08 °C. The PV power in Figure 13c varies continuously, with a peak of 1017 W. The battery power also fluctuates smoothly to maintain the load power and voltage constant at the selected values. The battery appears to be charging with values above 0 W (when PV power is sufficient for the load requirements) and discharging at values below 0 W (when PV power is insufficient for the load requirements).
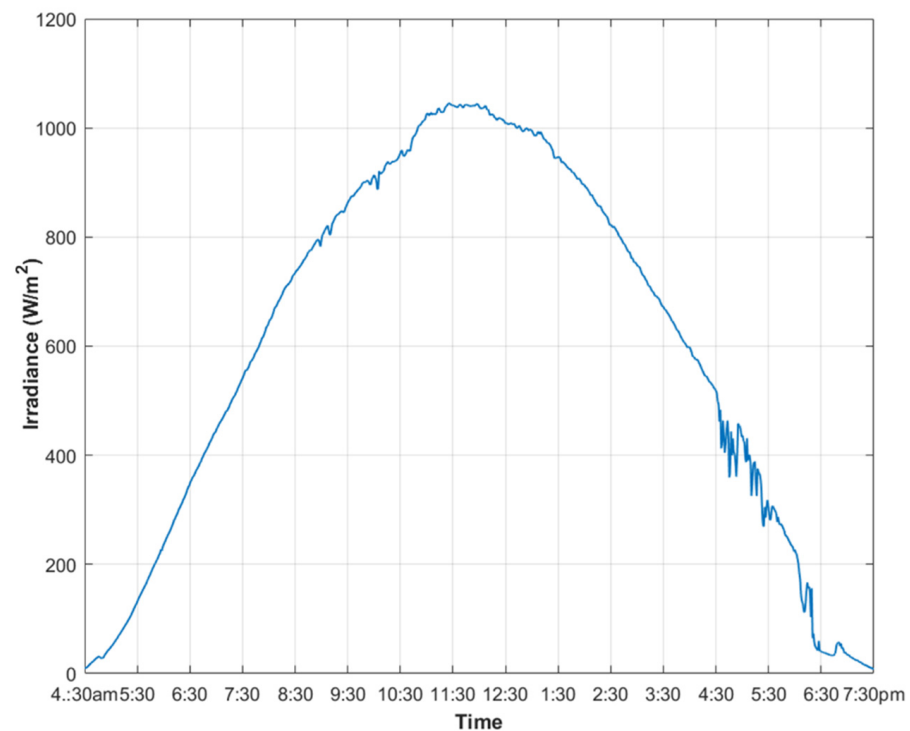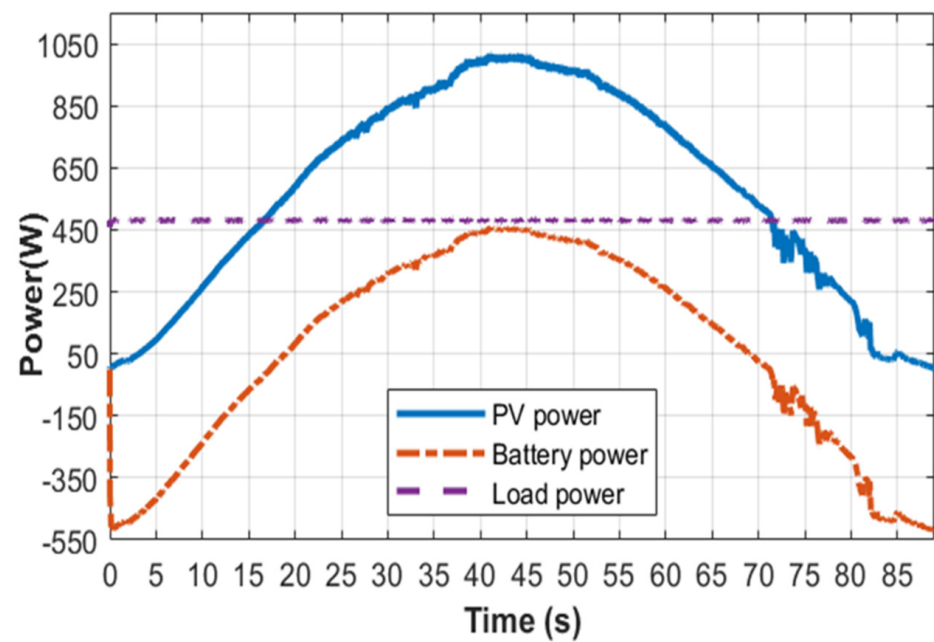

(**a**) Irradiance change

Figure 13. *Cont.*
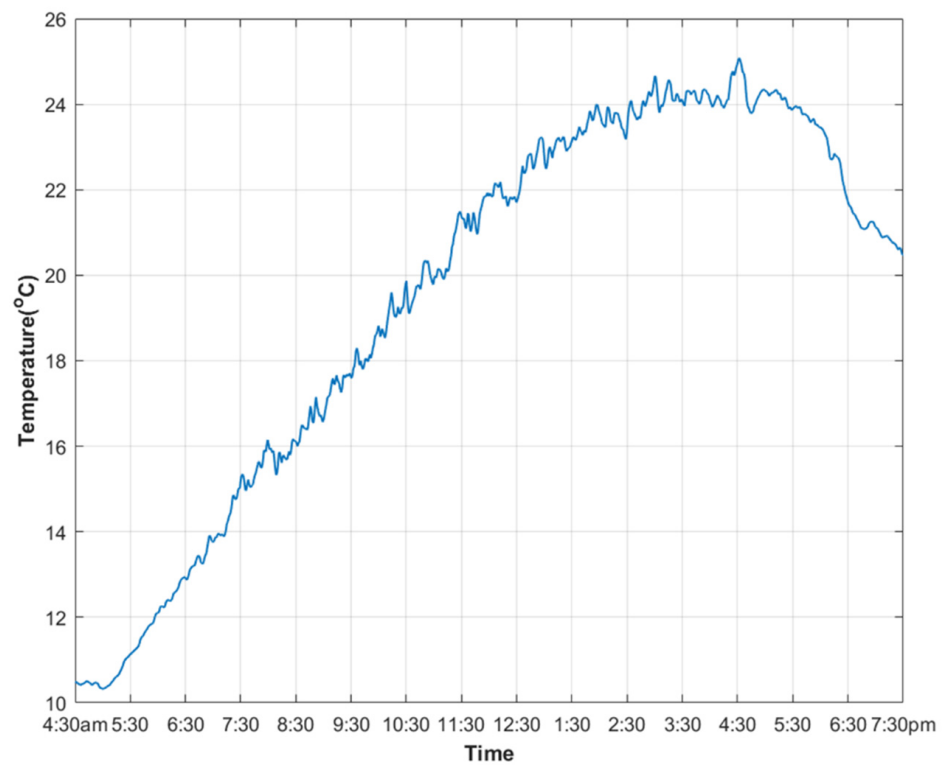
(**b**) Temperature change

(**c**) PV, battery, and load power

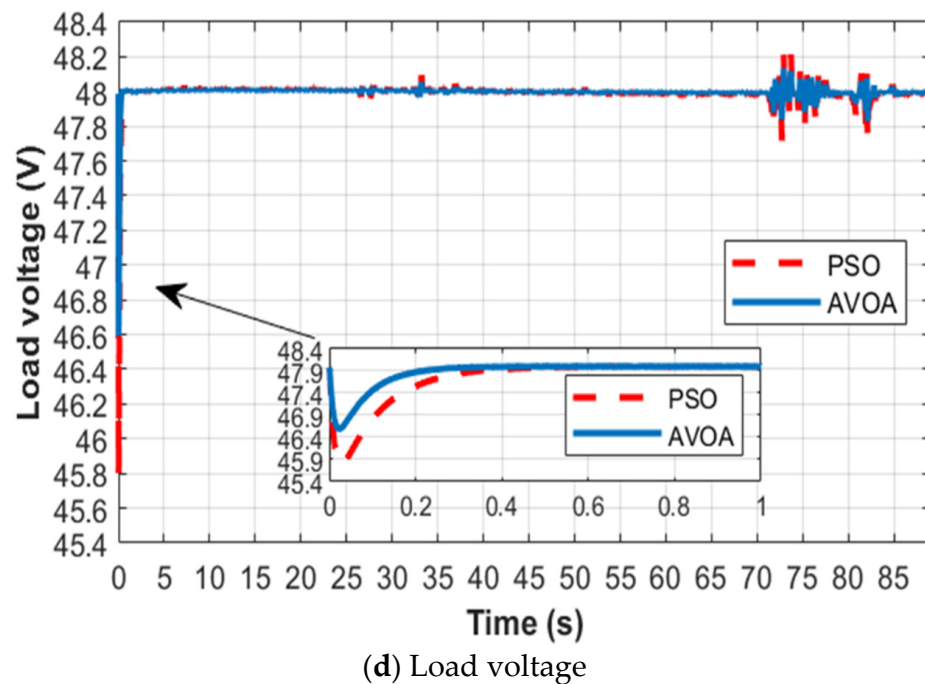**Figure 13.** *Cont.*

(d) Load voltage

Figure 13. (**a**) Irradiance change; (**b**) temperature change; (**c**) PV, battery, and load power; (**d**) Load voltage.

Results in Figure 13d show better performance for the AVOA than the PSO in terms of overshoot, undershoot, and settling time for the load voltage controlling while controlling the two PI controllers of the bidirectional DC/DC converter. It can be noticed that the RESs sudden penetration of the system caused an MPUS of 2.916% in the case of the AVOA and 4.583% in the case of PSO, a MPOS of 0.28% in the case of the AVOA and 0.43% with PSO, T_s of 0.35 s in the case of the AVOA and 0.58 with PSO; however, the controllers handled those fluctuations with a fast response to regain the system stability within the acceptable limits of voltage variation. This result indicates the advances of the AVOA over the PSO by about 37%, 34.89%, and 39.6% in this case for the MPUS, MPOS, and T_s parameters, respectively. Moreover, the BES system role is noticed in this case.

5.5. Case #5: PV Uncertainties from Real Data Accompanied by Load Perturbations

On June 8, 2022, irradiance and temperature fluctuates using actual data obtained from NREL's website at the Solar Radiation Research Laboratory [59], the same data used in case #4 Figure 13a–b with taking into consideration the influence of load uncertainty. In this instance, the load perturbation steps up at time = 20 s, increasing the burden by 10%. At time = 40 s, the load perturbation reaches 50% of the nominal load. At time = 50 s, the load perturbation decreases to 10% of the nominal load, and at time = 70 s, the load returns to its nominal value of 10A and 480 W. With a peak of 1017 W, the PV power in Figure 14a varies continually. The battery power swings smoothly with the PV variations to keep the load power and voltage constant at the chosen settings. When PV output is adequate to meet the demands of the load, the battery seems to be charging at values above 0 W, and when PV power is insufficient for the load requirements, the battery discharges at values below 0 W.
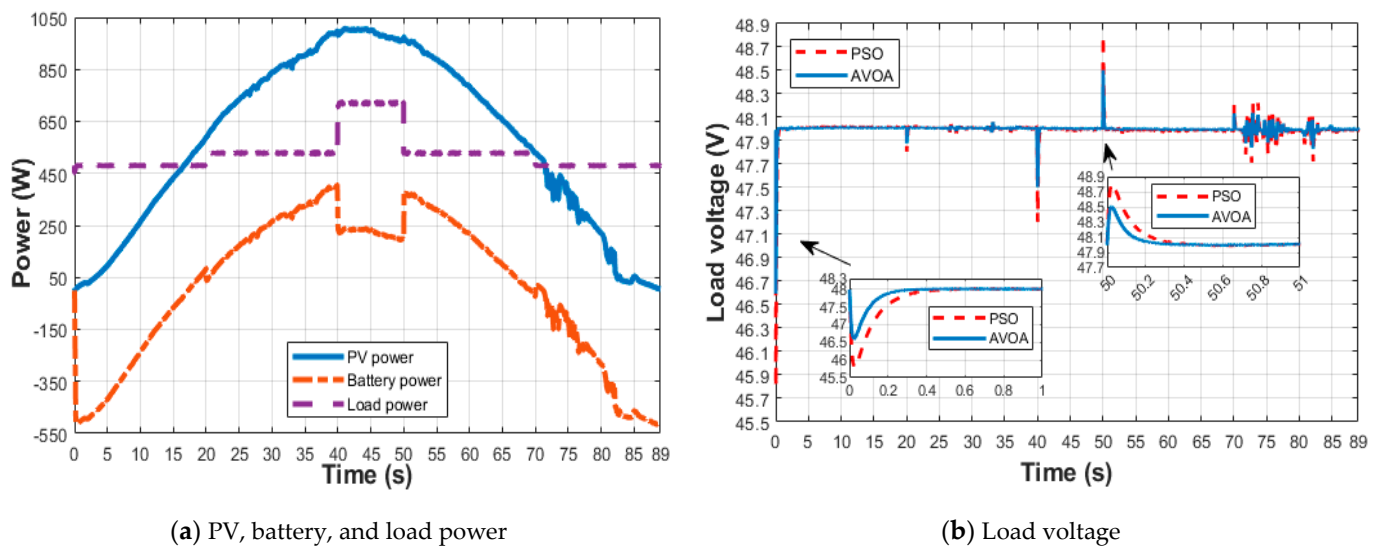
(**a**) PV, battery, and load power

(**b**) Load voltage

Figure 14. (**a**) PV, battery, and load power; (**b**) load voltage.

In terms of overshoot, undershoot, and settling time for controlling the load voltage while operating the two PI controllers of the bidirectional DC/DC converter, the results in Figure 14b demonstrate higher performance for the AVOA than the PSO. As can be seen, the sudden entry of RESs (PV) into the system resulted in a MPOS of 1.04% for the AVOA and 1.67% for PSO, a MPUS of 2.916% for the AVOA and 4.583% for PSO, and T_s of 0.38 s for the AVOA and 0.54 s for PSO. However, the controllers quickly responded to these fluctuations to restore system stability within acceptable voltage variation ranges. This result shows that the AVOA outperformed the PSO for the MPOS, MPUS, and Ts parameters by approximately 37.72%, 36.37%, and 29.6%, respectively. In this case, the BES system's function is also apparent.

5.6. Case #6: Fuel Cell Integrated into the PV-Battery System

A fuel cell of 650 W is added to the system with a PV of 1 kW integrated with the battery that has a capacity of 150 Ah. The FC is then connected to a boost converter to maintain the DC–bus voltage constant. The studied fuel cell parameters are presented in Table 2. This case has two PI controllers for the bidirectional converter of the battery and one PI controller for the boost converter of the fuel cell. This case did not consider solar uncertainties for irradiance and temperature fluctuations. It considered only step load change from 720 W at time = 1 s to 1440 W. The controllers' gains for this case are given in Table 8. The search area for the swarm particles and vulture population for the boost converter of the fuel cell are kept at the same $0 < k_p < 0.01$ and $0 < k_i < 0.4$ with the same gain ranges for the bidirectional converter controller mentioned in case #1 for fair comparisons.

Table 8. Microgrid's controller settings for case #4.

Gains	AVOA-Based			PSO-Based		
	PI$_1$	PI$_2$	PI$_3$	PI$_1$	PI$_2$	PI$_3$
K$_p$	10	0.0453	0.01	6.5692	0.5128	0.0061
K$_i$	150	80.0046	0.4	89.5336	130.5524	0.1596

The outcomes show the system stability and the role of the ES units. Figure 15a shows the coordination between system energy sources to supply the load. Figure 15b shows that the voltage regulation for the load voltage is within acceptable limits. This case outcome offers better performance for the AVOA in contrast to the implementation of the PSO through the indicators used to assess its performance in Table 9. The MPOS of

the load voltage is 5.01% in the AVOA while it is 6.135% in PSO, which indicates a MPUS enhancement by almost 18.34%. The MPUS of the load voltage is 3.95% in the AVOA and 8.604% in PSO, which presents an improvement in the MPOS by about 54.1%. T_s of the load voltage is 0.47 s in the AVOA while it is 0.93 s in PSO, so T_s has intensified by nearly 49.5%.
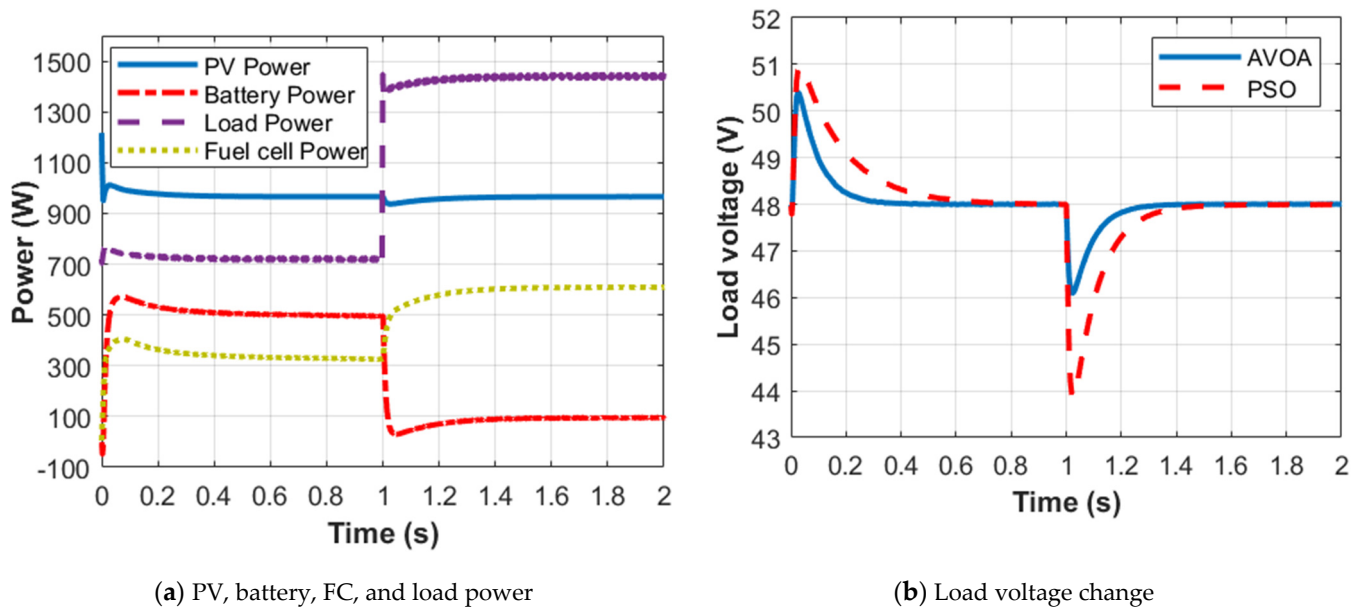

(**a**) PV, battery, FC, and load power

(**b**) Load voltage change

Figure 15. (**a**) PV, battery, FC, and load power; (**b**) load voltage change.

Table 9. Microgrid's transient parameters for load voltage.

	MPOS (%)	MPUS (%)	T_s (s)
AVOA	5.01	3.95	0.47
PSO	6.135	8.604	0.93

6. Conclusions

The RESs penetration caused problems for the islanded DC microgrid as voltage instability. This paper presents the cascaded double-loop control based on the PI controller designed through a new nature-inspired optimization technique, AVOA, to obtain the optimal settings for the PI controllers used. Two types of renewable energy sources are presented, PV and fuel cells, with the battery as an energy storage unit. The DC microgrid voltage stability is maintained within acceptable ranges of voltage fluctuations while subjected to actual irradiance, temperature changes, and sudden load dynamics. This study's used algorithms (AVOA and PSO) offer high flexibility and dependability, quick convergence, ease of implementation, strong robustness, and capability to manage the objective function [60]. However, PSO might converge to the minimum point locally [37]. The results show the robustness of the presented technique when compared with PSO to validate its performance and outcomes, including a lower overshoot and settling time via an overall percentage of improvement in the different indicators of the MPOS, MPUS, and T_s, which is about 38%. Moreover, the results demonstrate the role of the ES units in enhancing voltage regulation.

References

1. Lv, J.; Wang, X.; Wang, G.; Song, Y. Research on Control Strategy of Isolated DC Microgrid Based on SOC of Energy Storage System. *Electronics* **2021**, *10*, 834. [CrossRef]
2. Rawa, M.; Abusorrah, A.; Bassi, H.; Mekhilef, S.; Ali, Z.M.; Abdel Aleem, S.H.E.; Hasanien, H.M.; Omar, A.I. Economical-Technical-Environmental Operation of Power Networks with Wind-Solar-Hydropower Generation Using Analytic Hierarchy Process and Improved Grey Wolf Algorithm. *Ain Shams Eng. J.* **2021**, *12*, 2717–2734. [CrossRef]
3. Emara, D.; Ezzat, M.; Abdelaziz, A.Y.; Mahmoud, K.; Lehtonen, M.; Darwish, M.M.F. Novel Control Strategy for Enhancing Microgrid Operation Connected to Photovoltaic Generation and Energy Storage Systems. *Electronics* **2021**, *10*, 1261. [CrossRef]
4. Jyothi, V.M.; Muni, T.V.; Lalitha, S.V.N.L. An Optimal Energy Management System for PV/Battery Standalone System. *IJECE* **2016**, *6*, 2538. [CrossRef]
5. Yang, Y.; Qin, Y.; Tan, S.-C.; Hui, S.Y.R. Efficient Improvement of Photovoltaic-Battery Systems in Standalone DC Microgrids Using a Local Hierarchical Control for the Battery System. *IEEE Trans. Power Electron.* **2019**, *34*, 10796–10807. [CrossRef]
6. Xu, Q.; Vafamand, N.; Chen, L.; Dragicevic, T.; Xie, L.; Blaabjerg, F. Review on Advanced Control Technologies for Bidirectional DC/DC Converters in DC Microgrids. *IEEE J. Emerg. Sel. Topics Power Electron.* **2021**, *9*, 1205–1221. [CrossRef]
7. Nguyen, T.L.; Guerrero, J.M.; Griepentrog, G. A Self-Sustained and Flexible Control Strategy for Islanded DC Nanogrids Without Communication Links. *IEEE J. Emerg. Sel. Topics Power Electron.* **2020**, *8*, 877–892. [CrossRef]
8. Hussien, A.M.; Hasanien, H.M.; Mekhamer, S.F. Sunflower Optimization Algorithm-Based Optimal PI Control for Enhancing the Performance of an Autonomous Operation of a Microgrid. *Ain Shams Eng. J.* **2021**, *12*, 1883–1893. [CrossRef]
9. Chen, X.; Shi, M.; Zhou, J.; Zuo, W.; Chen, Y.; Wen, J.; He, H. Consensus-Based Distributed Control for Photovoltaic-Battery Units in a DC Microgrid. *IEEE Trans. Ind. Electron.* **2019**, *66*, 7778–7787. [CrossRef]
10. Dashtdar, M.; Flah, A.; El-Bayeh, C.Z.; Tostado-Véliz, M.; Al Durra, A.; Abdel Aleem, S.H.E.; Ali, Z.M. Frequency Control of the Islanded Microgrid Based on Optimised Model Predictive Control by PSO. *IET Renew. Power Gen* **2022**, *16*, 2088–2100. [CrossRef]
11. Ould Amrouche, S.; Rekioua, D.; Rekioua, T.; Bacha, S. Overview of Energy Storage in Renewable Energy Systems. *Int. J. Hydrogen Energy* **2016**, *41*, 20914–20927. [CrossRef]
12. Lukačević, O.; Almalaq, A.; Alqunun, K.; Farah, A.; Ćalasan, M.; Ali, Z.M.; Aleem, S.H. Optimal CONOPT solver-based coordination of bi-directional converters and energy storage systems for regulation of active and reactive power injection in modern power networks. *Ain Shams Eng. J.* **2022**, *13*, 101803. [CrossRef]
13. Kumar, M.; Hote, Y.V. Maximum Sensitivity-Constrained Coefficient Diagram Method-Based PIDA Controller Design: Application for Load Frequency Control of an Isolated Microgrid. *Electr. Eng.* **2021**, *103*, 2415–2429. [CrossRef]
14. Khodamoradi, A.; Liu, G.; Mattavelli, P. Online Controller Tuning for DC Microgrid Power Converters With the Ability to Track Maximum Allowable Bandwidth. *IEEE Trans. Ind. Electron.* **2022**, *69*, 1888–1897. [CrossRef]
15. Wu, M.; Lu, D.D.-C. A Novel Stabilization Method of LC Input Filter With Constant Power Loads Without Load Performance Compromise in DC Microgrids. *IEEE Trans. Ind. Electron.* **2015**, *62*, 4552–4562. [CrossRef]
16. Zhang, X.; Ruan, X.; Zhong, Q.-C. Improving the Stability of Cascaded DC/DC Converter Systems via Shaping the Input Impedance of the Load Converter With a Parallel or Series Virtual Impedance. *IEEE Trans. Ind. Electron.* **2015**, *62*, 7499–7512. [CrossRef]
17. Kwasinski, A.; Onwuchekwa, C.N. Dynamic Behavior and Stabilization of DC Microgrids With Instantaneous Constant-Power Loads. *IEEE Trans. Power Electron.* **2011**, *26*, 822–834. [CrossRef]
18. Braitor, A.-C.; Konstantopoulos, G.C.; Kadirkamanathan, V. Current-Limiting Droop Control Design and Stability Analysis for Paralleled Boost Converters in DC Microgrids. *IEEE Trans. Contr. Syst. Technol.* **2021**, *29*, 385–394. [CrossRef]
19. Bracale, A.; Caramia, P.; Carpinelli, G.; Mancini, E.; Mottola, F. Optimal Control Strategy of a DC Micro Grid. *Int. J. Electr. Power Energy Syst.* **2015**, *67*, 25–38. [CrossRef]

20. Hatahet, W.; Mokhtar, M.; Marei, M.I. Performance Enhancing of Grid-Connected DC Microgrid. In Proceedings of the 2019 IEEE Conference on Power Electronics and Renewable Energy (CPERE), Aswan City, Egypt, 23–25 October 2019; IEEE: Aswan City, Egypt, 2019; pp. 361–366. [CrossRef]

21. Kim, D.-E. Power Flow Study of Low-Voltage DC Micro-Grid and Control of Energy Storage System in the Grid. *J. Electr. Eng. Technol.* **2017**, *12*, 549–558. [CrossRef]

22. Ríos, S.J.; Pagano, D.J.; Lucas, K.E. Bidirectional Power Sharing for DC Microgrid Enabled by Dual Active Bridge DC-DC Converter. *Energies* **2021**, *14*, 404. [CrossRef]

23. Peng, J.; Fan, B.; Yang, Q.; Liu, W. Fully Distributed Discrete-Time Control of DC Microgrids With ZIP Loads. *IEEE Syst. J.* **2022**, *16*, 155–165. [CrossRef]

24. Hasanien, H.M.; Matar, M. A Fuzzy Logic Controller for Autonomous Operation of a Voltage Source Converter-Based Distributed Generation System. *IEEE Trans. Smart Grid* **2015**, *6*, 158–165. [CrossRef]

25. Elsisi, M.; Tran, M.-Q.; Hasanien, H.M.; Turky, R.A.; Albalawi, F.; Ghoneim, S.S.M. Robust Model Predictive Control Paradigm for Automatic Voltage Regulators against Uncertainty Based on Optimization Algorithms. *Mathematics* **2021**, *9*, 2885. [CrossRef]

26. Shan, Y.; Hu, J.; Chan, K.W.; Fu, Q.; Guerrero, J.M. Model Predictive Control of Bidirectional DC–DC Converters and AC/DC Interlinking Converters—A New Control Method for PV-Wind-Battery Microgrids. IEEE Trans. Sustain. *Energy* **2019**, *10*, 1823–1833. [CrossRef]

27. Sobhy, M.A.; Abdelaziz, A.Y.; Hasanien, H.M.; Ezzat, M. Marine Predators Algorithm for Load Frequency Control of Modern Interconnected Power Systems Including Renewable Energy Sources and Energy Storage Units. *Ain Shams Eng. J.* **2021**, *12*, 3843–3857. [CrossRef]

28. Ma, R.; Xu, L.; Xie, R.; Zhao, D.; Huangfu, Y.; Gao, F. Advanced Robustness Control of DC–DC Converter for Proton Exchange Membrane Fuel Cell Applications. *IEEE Trans. Ind. Applicat.* **2019**, *55*, 6389–6400. [CrossRef]

29. Ang, K.H.; Chong, G.; Yun, L. P.I.D. Control System Analysis, Design, and Technology. *IEEE Trans. Contr. Syst. Technol.* **2005**, *13*, 559–576. [CrossRef]

30. Hussien, A.M.; Mekhamer, S.F.; Hasanien, H.M. Cuttlefish Optimization Algorithm Based Optimal PI Controller for Performance Enhancement of an Autonomous Operation of a DG System. In Proceedings of the 2020 2nd International Conference on Smart Power & Internet Energy Systems (SPIES), Bangkok, Thailand, 15 September 2020; pp. 293–298. [CrossRef]

31. Shaheen, M.A.M.; Mekhamer, S.F.; Hasanien, H.M.; Talaat, H.E.A. Optimal Power Flow of Power Systems Using Hybrid Firefly and Particle Swarm Optimization Technique. In Proceedings of the 2019 21st International Middle East Power Systems Conference (MEPCON), Cairo, Egypt, 17–19 December 2019; pp. 232–237.

32. Muhammad, M.A.; Mokhlis, H.; Naidu, K.; Amin, A.; Franco, J.F.; Othman, M.A. Distribution Network Planning Enhancement via Network Reconfiguration and DG Integration Using Dataset Approach and Water Cycle Algorithm. *J. Mod. Power Syst. Clean Energy* **2020**, *8*, 86–93. [CrossRef]

33. Hasanien, H.M.; Matar, M. Water Cycle Algorithm-based Optimal Control Strategy for Efficient Operation of an Autonomous Microgrid. *IET Gener. Transm. Distrib.* **2018**, *12*, 5739–5746. [CrossRef]

34. Mahmoud, H.Y.; Hasanien, H.M.; Besheer, A.H.; Abdelaziz, A.Y. Hybrid Cuckoo Search Algorithm and Grey Wolf Optimiser-based Optimal Control Strategy for Performance Enhancement of HVDC-based Offshore Wind Farms. *IET Gener. Transm. Distrib.* **2020**, *14*, 1902–1911. [CrossRef]

35. Helmi, A.M.; Carli, R.; Dotoli, M.; Ramadan, H.S. Efficient and Sustainable Reconfiguration of Distribution Networks via Metaheuristic Optimization. *IEEE Trans. Autom. Sci. Eng.* **2021**, *19*, 21525153. [CrossRef]

36. Qais, M.H.; Hasanien, H.M.; Alghuwainem, S. Parameters Extraction of Three-Diode Photovoltaic Model Using Computation and Harris Hawks Optimization. *Energy* **2020**, *195*, 117040. [CrossRef]

37. Elazab, O.S.; Debouza, M.; Hasanien, H.M.; Muyeen, S.M.; Al-Durra, A. Salp Swarm Algorithm-based Optimal Control Scheme for LVRT Capability Improvement of Grid-connected Photovoltaic Power Plants: Design and Experimental Validation. *IET Renew. Power Gener.* **2020**, *14*, 591–599. [CrossRef]

38. Hussien, A.M.; Turky, R.A.; Alkuhayli, A.; Hasanien, H.M.; Tostado-Veliz, M.; Jurado, F.; Bansal, R.C. Coot Bird Algorithms-Based Tuning PI Controller for Optimal Microgrid Autonomous Operation. *IEEE Access* **2022**, *10*, 6442–6458. [CrossRef]

39. Rashid, M.H. (Ed.) *Power Electronics Handbook: Devices, Circuits, and Applications Handbook*, 3rd ed.; Elsevier: Burlington, MA, USA, 2011; ISBN 9780123820365.

40. Chao, K.; Tseng, M.-C.; Huang, C.; Liu, G.; Huang, L.-C. Design and Implementation of a Bidirectional DC-DC Converter for Stand-Alone Photovoltaic Systems. *Energy* **2013**, *4*, 8.

41. Ahamed, M.H.F.; Dissanayake, U.D.S.D.; De Silva, H.M.P.; Kumara, H.R.C.G.P.; Lidula, N.W.A. Designing and Simulation of a DC Microgrid in PSCAD. In Proceedings of the 2016 IEEE International Conference on Power System Technology (POWERCON), Wollongong, Australia, 28 September 1–October 2016; pp. 1–6.

42. Scarabaggio, P.; Carli, R.; Dotoli, M. Noncooperative Equilibrium Seeking in Distributed Energy Systems Under AC Power Flow Nonlinear Constraints. *IEEE Trans. Control Netw. Syst.* **2022**, 1–12. [CrossRef]

43. Yao, M.; Molzahn, D.K.; Mathieu, J.L. An Optimal Power-Flow Approach to Improve Power System Voltage Stability Using Demand Response. *IEEE Trans. Control Netw. Syst.* **2019**, *6*, 1015–1025. [CrossRef]

44. Li, J.; Liu, F.; Wang, Z.; Low, S.H.; Mei, S. Optimal Power Flow in Stand-Alone DC Microgrids. *IEEE Trans. Power Syst.* **2018**, *33*, 5496–5506. [CrossRef]

45. Morstyn, T.; Hredzak, B.; Agelidis, V.G. Dynamic Optimal Power Flow for DC Microgrids with Distributed Battery Energy Storage Systems. In Proceedings of the 2016 IEEE Energy Conversion Congress and Exposition (ECCE), Milwaukee, WI, USA, 18–22 September 2016; pp. 1–6.

46. Zafeiratou, I.; Prodan, I.; Lefévre, L. A Hierarchical Control Approach for Power Loss Minimization and Optimal Power Flow within a Meshed DC Microgrid. *Energies* **2021**, *14*, 4846. [CrossRef]

47. Li, C.; de Bosio, F.; Chaudhary, S.K.; Graells, M.; Vasquez, J.C.; Guerrero, J.M. Operation Cost Minimization of Droop-Controlled DC Microgrids Based on Real-Time Pricing and Optimal Power Flow. In Proceedings of the IECON 2015-41st Annual Conference of the IEEE Industrial Electronics Society, Yokohama, Japan, 9–12 November 2015; pp. 003905–003909.

48. Qais, M.H.; Hasanien, H.M.; Alghuwainem, S.; Loo, K.H.; Elgendy, M.A.; Turky, R.A. Accurate Three-Diode Model Estimation of Photovoltaic Modules Using a Novel Circle Search Algorithm. *Ain Shams Eng. J.* **2022**, *13*, 101824. [CrossRef]

49. Abdel, H.E.; Aleem, S. Towards Developing A Unified Index For Power Quality Evaluation In Distributed Generation Systems. *Sci. Trends* **2018**, *149*, 607–622. [CrossRef]

50. Ibrahim, O.; Yahaya, N.Z.; Saad, N.; Umar, M.W. Matlab/Simulink Model of Solar PV Array with Perturb and Observe MPPT for Maximising PV Array Efficiency. In Proceedings of the 2015 IEEE Conference on Energy Conversion (CENCON), Johor Bahru, Malaysia, 19–20 October 2015; pp. 254–258.

51. Qais, M.H.; Hasanien, H.M.; Turky, R.A.; Alghuwainem, S.; Loo, K.-H.; Elgendy, M. Optimal PEM Fuel Cell Model Using a Novel Circle Search Algorithm. *Electronics* **2022**, *11*, 1808. [CrossRef]

52. Dwivedi, Y.; Kumar Tayal, V. Dynamic Stability Improvement of Alkali Fuel Cell Integrated System Using PSO Optimized PID. Control Design. In Proceedings of the 2017 Recent Developments in Control, Automation & Power Engineering (RDCAPE), Noida, India, 26–27 October 2017; pp. 499–504.

53. Yakout, A.H.; Hasanien, H.M.; Kotb, H. Proton Exchange Membrane Fuel Cell Steady State Modeling Using Marine Predator Algorithm Optimizer. *Ain Shams Eng. J.* **2021**, *12*, 3765–3774. [CrossRef]

54. Gandoman, F.H.; Ahmed, E.M.; Ali, Z.M.; Berecibar, M.; Zobaa, A.F.; Aleem, A. SHE Reliability Evaluation of Lithium-Ion Batteries for E-Mobility Applications from Practical and Technical Perspectives: A Case Study. *Sustainability* **2021**, *13*, 11688. [CrossRef]

55. Hemeida, A.M.; El-Ahmar, M.H.; El-Sayed, A.M.; Hasanien, H.M.; Alkhalaf, S.; Esmail, M.F.C.; Senjyu, T. Optimum Design of Hybrid Wind/PV Energy System for Remote Area. *Ain Shams Eng. J.* **2020**, *11*, 11–23. [CrossRef]

56. Ferreira, R.A.; Braga, H.A.; Ferreira, A.A.; Barbosa, P.G. Analysis of voltage droop control method for dc microgrids with Simulink: Modelling and simulation. In Proceedings of the 2012 10th IEEE/IAS International Conference on Industry Applications, Fortaleza, Brazil, 5–7 November 2012; Volume 11, pp. 1–6.

57. Abdollahzadeh, B.; Gharehchopogh, F.S.; Mirjalili, S. African Vultures Optimization Algorithm: A New Nature-Inspired Metaheuristic Algorithm for Global Optimization Problems. *Comput. Ind. Eng.* **2021**, *158*, 107408. [CrossRef]

58. Sumaiya, S. Modeling, Designing and Analysis of a Standalone PV DC Microgrid System. Master's Thesis, Georgia Southern University, Statesboro, GA, USA, 2018.

59. Stoffel, T.; Andreas, A. *NREL Solar Radiation Research Laboratory (SRRL): Baseline Measurement System (BMS)*; NREL Report No. DA-5500-564881; NREL Solar Radiation Research Laboratory: Golden, CL, USA, 1981. [CrossRef]

60. Sayed, A.; Ebeed, M.; Ali, Z.M.; Abdel-Rahman, A.B.; Ahmed, M.; Abdel Aleem, S.H.E.; El-Shahat, A.; Rihan, M. A Hybrid Optimization Algorithm for Solving of the Unit Commitment Problem Considering Uncertainty of the Load Demand. *Energies* **2021**, *14*, 8014. [CrossRef]